

Controlling the snap-through behavior of kirigami arches

Eszter Fehér^{a,b}

^a*Department of Morphology and Geometric Modeling, Műegyetem rkp. 1-3, Budapest, 1111, Hungary*
^b*HUN-REN-BME Morphodynamics Research Group, Műegyetem rkp. 1-3, Budapest, 1111, Hungary*

Abstract

This work examines the snap-through behavior of clamped-clamped kirigami arches made from initially flat, thin, cut sheets under increasing vertical concentrated load acting at midspan. A two-parameter, symmetric pattern is introduced to conduct a numerical parameter analysis across three different support distances. When the support distance is one-quarter of the total length of the sheet, the structure loses stability at a symmetry point bifurcation over a wide range of parameters. Additionally, there exists a small range of parameters where limit point bifurcation occurs. In this case, the cuts can induce symmetry in the stability loss. For larger support distances (half or three-quarters of the total length), limit point bifurcation occurs only for small cuts, and there is a range of cut parameters that leads to monotonic monostability, indicating that no stability loss occurs. These findings are supported by experimental data. Overall, our research demonstrates that carefully designed cut patterns can either control the mode of stability loss in kirigami arches or suppress it entirely.

Keywords: kirigami, arch, snap-through, stability, bifurcation, elastica

1. Introduction

The paper technique known as kirigami has recently gained significant interest due to its ability to create three-dimensional structures from flat sheets through cutting and folding. This technique has a wide range of engineering applications, including ventilation systems (Stein-Montalvo et al., 2024), space structures (Pedivellano and Pellegrino, 2024), evaporator systems (Li et al., 2024), biomedical devices (Wu et al., 2025), soft robotics (Hong et al., 2022), electronics (Liu et al., 2022), and metamaterials (Hamzehei et al., 2024). Since these structures are made from flat sheets, they are material-efficient, easy to transport, and ideal for deployable designs.

The location and shape of the cuts enable the achievement of specific shapes or mechanical properties. Shrimali et al. (2021) investigated how the perforation of a plate can alter its bending properties. Similarly, cuts made on inextensible sheets can induce various mechanical properties, such as stretchability, auxetic behavior, and programmable kinematics (Tao et al., 2023). Furthermore, kirigami structures can lose their stability while still remaining functional or even gain new functionalities. It is possible to design the mode of stability loss of and the behavior that follows (Rafsanjani and Bertoldi, 2017; Du et al., 2024). This design approach

allows dome-shaped kirigami shells to switch between multiple stable states through a snap-through mechanism (Yang et al., 2024; Cho and Kim, 2023).

One of the simplest kirigami patterns consists of flat strips. When the ends of these strips are brought together, they buckle out of the plane, forming an elastica shape (Lee et al., 2022; Hong et al., 2022). By perforating the sheet or introducing additional cuts, we can alter the geometry (Zhang et al., 2022; Liu et al., 2020) or the structural rigidity of an individual kirigami arch (Fehér and Gyetvai, 2024; Fehér, 2025). However, there is still a lack of literature exploring the relationship between cut patterns and the stability properties of kirigami arches.

The literature on the stability of arches is extensive. Timoshenko and Gere (1961) focused on determining the critical buckling load of curved, circular arches. Pi and Trahair (1998) and later Pi et al. (2002) analyzed the stability behavior shallow circular arches. Luu and Lee (2016) explored elliptical arches with various support conditions and identified different types of buckling, including cases where no buckling occurred. Their findings indicated that non-slender structures and shallow arches did not experience buckling.

There are also several studies related to the stability properties of the elastica. For instance, Chen and

Hung (2011) conducted a snap-through analysis of an elastica subjected to a concentrated vertical load, where the supports are hinges. The analysis revealed that different load conditions lead to varying stability properties, such as sub-critical pitchfork bifurcation (symmetry point bifurcation) or limit point bifurcation. Additionally, Zhang et al. (2025) explored the snap-through behavior of a heavy, hard magnetic elastica. Gomez et al. (2017) investigated the dynamics of a snapping elastica, while Liu and Burgueño (2016) focused on a constrained elastica designed as an energy harvester. Furthermore, Cheng et al. (2023) examined the buckling behavior of compressed, constrained ribbons under vertical loading, and Zhang et al. (2020) investigated the buckling modes of buckled ribbons when subjected to vertical loads. None of these works considered the effects of cuts introduced in the geometry.

In this study, we investigate the snap-through instability of kirigami arches depending on various cut patterns. Our analysis focuses on a clamped-clamped kirigami arch made from an initially flat, thin, rectangular sheet, which is subjected to a vertical concentrated load at its midpoint. We introduce a simple, two-parameter, symmetric cut pattern consisting of two rectangular cuts placed along the longer edges of the sheet. Our objective is to show that the cut pattern can control the stability behavior of the arch. To achieve this, we conduct a numerical parameter analysis and compare our findings with experimental results.

The paper is structured as follows: Section 2 outlines the mechanical model and numerical approach, Section 3 presents the numerical and experimental results along with their discussion, and Section 4 concludes the paper.

2. Methodology

2.1. Mechanical background

We consider a thin, initially flat rectangular sheet with thickness t , length L , and width W . The sheet has two transversally symmetric rectangular holes positioned at the center of its longer edges, characterized by parameters a and b (Fig. 1a). The sheet is forced to take an arched shape by bringing its ends closer together at a distance of $B < L$ and fixing them at vertical positions (Fig. 1b). Two horizontal forces F_x are applied at the ends of the sheet to maintain equilibrium in the arched form. Additionally, the sheet carries its self-weight p , along with a concentrated load P acting at the midpoint. If all the parameters are fixed, the cut pattern determines the shape of the arch. In general, as the concentrated load P is increased, the structural height decreases, and

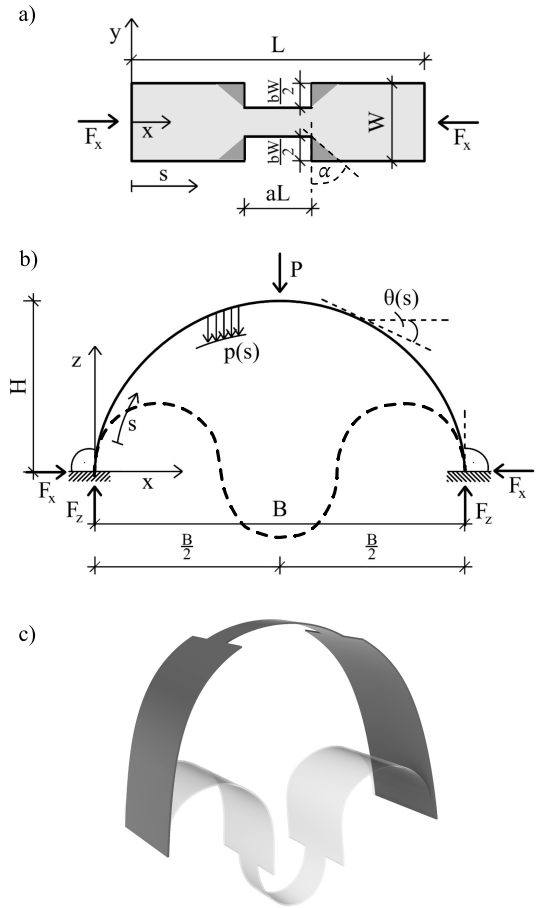


Figure 1: a) Illustration of the cut pattern and its parameters a and b . Dark grey regions are considered to be stress-free, and they are neglected in the calculation of the effective moment of inertia of the sheet. b) Mechanical model of the structure. The dashed thick line is the inverted shape after snap-through. c) Three-dimensional visualization of the structure in the initial state ($P = 0$) and after snap-through ($P > P_{crit}$).

the shape loses stability at P_{crit} . If the supports are not too close to each other, the structure takes an inverted shape (Fig. 1b,c). This phenomenon is called the snap-through.

We consider quasi-static loading, examining both stable and unstable equilibrium states, and do not consider the dynamic aspects of snap-through. Due to the small thickness and transverse symmetry of the sheet, we can use a nonlinear beam model, the elastica equation, to describe the deformations of the sheet. The sheet is parameterized by its arc-length $s \in [0, L]$ and the deformations are described by the tangent angle $\theta(s)$. The concentrated load acts at $s_P = L/2$. The moment equi-

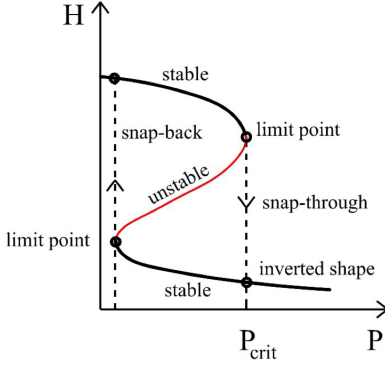


Figure 2: Schematic load-height diagram visualizing a limit point bifurcation. Red and black denote the unstable and stable points, respectively.

librium equation (Howell et al., 2009) is:

$$E \frac{d}{ds} \left[I_{\text{eff}}(s) \frac{d\theta(s)}{ds} \right] - F_z \cos \theta(s) + F_x \sin \theta(s) + \cos \theta(s) \int_0^s Q p(s) ds + P \cos \theta(s) \hat{H}(s - s_p) = 0, \quad (1)$$

where E is the Young's modulus; $I_{\text{eff}}(s)$ is the effective moment of inertia; \hat{H} is the Heavyside function; $p(s)$ is the self-weight distribution, normalized such that $\int_0^L p(s) ds = 1$ and scaled by the load intensity Q ; P is the concentrated vertical load; F_x and F_z are the horizontal and vertical support reactions, respectively. We assume that some parts of the sheet near the cuts do not contribute to carrying the loads. These regions form isosceles right triangles that are removed from the cross-section (Fig. 1a). The effective width of the sheet $w_{\text{eff}}(s)$ is the remaining width after the removal of these triangles. The corresponding effective moment of inertia is $I_{\text{eff}} = w_{\text{eff}}(s)^3 / 12$.

There are four boundary conditions

$$\theta(0) = \pi/2, \quad (2)$$

$$\theta(L) = -\pi/2, \quad (3)$$

$$x(L) = \int_0^L \cos(\theta(s)) ds = B, \quad (4)$$

$$z(L) = \int_0^L \sin(\theta(s)) ds = 0. \quad (5)$$

prescribing the tangent and the position of the sheet at the supports, respectively.

The structural height H is the vertical position of the midpoint, i.e., $H = z(L/2)$. The load-height diagram of the system is shown in Fig. 2. During unloading, the

load gradually decreases, and the inverted shape loses stability at a limit point, resulting in the so-called snap-back. An unstable set of points connects the upper and lower stable parts of the diagram.

Depending on the distance between the supports, even though the setup is symmetric, the stability loss might be possible before the limit point. In this case, the symmetric solution becomes unstable, and the structure passes through non-symmetric shapes before settling at a lower stable position (Thompson and Hunt, 1973), a phenomenon called symmetric point bifurcation.

It is important to note that our problem has some physical constraints that are not incorporated in the model. The beam model (Eq. 1) permits self-intersections, and the supports restrict only the positions of the endpoints (Eqs. 2–5), without imposing any limitations on the internal points. Consequently, points of the arch may pass through the supports in the model. This additional freedom requires extra caution when comparing the results with experimental observations.

2.2. Numerical procedure

Equation (1) has no analytical solution in the general case. To compute both stable and unstable equilibrium configurations, we use a combination of Chebyshev polynomial approximation and numerical continuation, a methodology previously successfully applied by Fehér et al. (2026) to determine equilibrium shapes of a curved rod under distributed loading. The structure is discretized by n points, and the derivatives of θ are approximated by derivatives of Chebyshev polynomials using Chebfun (Driscoll et al., 2014) in Matlab.

The Chebyshev approximation converges exponentially to the target function as n increases, even for the derivatives (Trefethen, 2000). However, the cut pattern needs to be considered when choosing the discretization. We selected $n = 340$, which provides sufficient resolution even in the vicinity of the cuts. Convergence tests supported this value. The boundary conditions given by Eqs. (2) and (3) were applied directly in the n resulting equations, and we added two additional equations for Eqs. (4) and (5). This leads to a total of $n + 2$ equations.

The resulting system of equations was solved via numerical continuation using pde2path (Dohnan et al., 2014; Uecker, 2021), treating F_x and F_z as free parameters. First, we start from a stable initial configuration with $P = Q = 0$, and perform continuation in B until the target value is achieved. Subsequently, B is fixed at its target level, and the continuation proceeds in Q . In the final step, we take P as the continuation parameter

and track the eigenvalues of the Jacobian of the system. Eigenvalues with negative real parts indicate unstable solutions (Uecker, 2021). A bifurcation point occurs when an eigenvalue crosses zero, and its location is determined using bisection. The tolerance for the residual is set to 10^{-8} , and the maximum step size was 1/20 of the target parameter value.

Using this procedure, we calculated the $H - P$ diagrams for various support distances, as well as different a and b values, and determined the corresponding critical loads.

3. Results and discussion

3.1. Parameter study

We generated cut patterns with $0.05 \leq a \leq 0.95$ and $0.05 \leq b \leq 0.95$ and computed the load-height diagram for three different support distances: $B = 0.25L$, $0.5L$, and $0.75L$. The resulting critical loads in terms of the pattern parameters are shown in Fig. 3. Interestingly, some patterns exhibited no snap-through at all for $B = 0.5$ and $B = 0.75L$, indicating monotonic monostability. These cases correspond to the white regions in Fig. 3b-c.

As expected, smaller cuts generally lead to higher critical loads, and the largest cut ($a = b = 0.95$) resulted in the lowest critical load for all B values. However, the decrease rate of P_{crit} is not uniform across the parameter range. This behavior can be linked to the resulting arch geometries. Small a and large b values are cuts that behave similarly to hinges in the structure. Previous work (Fehér, 2025) showed, that certain cut configurations can lead to structurally preferable shapes under a given load. Thus, while the smallest cut indeed yields the highest critical load, the favorable geometric effect of hinge-like cuts mitigates the weakening expected for patterns with small a values.

Figure 4 represents the $P - b - H$ equilibrium surfaces for all investigated support distances for three representative cut lengths $a = 0.3, 0.5, 0.7$. Stable and unstable states are marked in grey and red, respectively. The upper boundary of the red region corresponds to the P_{crit} values. The small waves on the surfaces are likely numerical artifacts associated with the computation of w_{eff} and the discretization with n points. Even though each a, b pair corresponds to cuts begin and end at mesh points, this may no longer hold once the edges are trimmed by α (Fig. 1a) to calculate I_{eff} .

Sections of the equilibrium surfaces corresponding to $a = 0.5$ (middle row of Fig. 4) are presented in Fig. 5 for $b = 0.1, 0.3, 0.5, 0.7$, and 0.9 .

3.2. Limit point bifurcation ($B = 0.5L, B = 0.75L$)

For $B = 0.5L, a = 0.5, 0.7$ and $B = 0.75L, a = 0.3, 0.5, 0.7$, we observe that the unstable region in Fig. 4 diminishes as b increases. In these cases, the equilibrium surfaces progressively flatten out, and the limit points vanish as b becomes large (Fig. 5). The surface does not flatten out in the case of $B = 0.5L, a = 0.3$ since the $a = 0.5$ vertical line does not cross the white region in Fig. 3b. Monotonic monostability occurs only for a certain range of parameters.

Previous studies have shown that monotonic monostability can also be achieved in circular curved beams by reducing slenderness or height (Luu and Lee, 2016). A possible explanation for the transition from snap-through monostability to monotonic monostability, as seen in Figs. 4-5, lies in the change in the arch geometry. Local weakening alters the unloaded shape, which can in turn modify the stability characteristics. Softened regions have lower bending resistance, allowing the structure to deform smoothly without reaching a limit point. Moreover, snap-through requires an initially stiff response. Softening the structure reduces the initial resistance, flattening the force-height curve and causing the limit point to disappear.

3.3. Symmetry point bifurcation ($B = 0.25L$)

In this subsection, we take a closer look at the case of $B = 0.25L$, that significantly differs from the other two analyzed support distances.

Figure 4 shows that the unstable region starts before the fold points for nearly all values of a and b . For $a = 0.5$, increasing b causes the surface to flatten out at the top, and a new limit point emerges in the middle, where the stability loss coincides with a limit point. For $a = 0.7$, although the surface also tends to flatten, the unstable region does not decrease significantly.

Consequently, not only symmetry point bifurcation but also limit point bifurcation can occur for this support distance. These two modes can be distinguished numerically by checking whether the onset of negative eigenvalues of the Jacobian coincides with the limit points, i.e., the location of the extreme values of the $H - P$ function. Figure 6 shows the mode of bifurcation in the $a - b$ parameter space, where grey and white regions correspond to limit point and symmetry point bifurcations, respectively. A set of representative load-height diagrams is shown as inset figures.

The $P - H$ diagrams we presented so far correspond only to the symmetric branch. However, the numerical tool we use allows branch switching at bifurcation points. Fig. 7a presents both the symmetric and asymmetric branches for $a = 0.4, b = 0.4$. The asymmetric

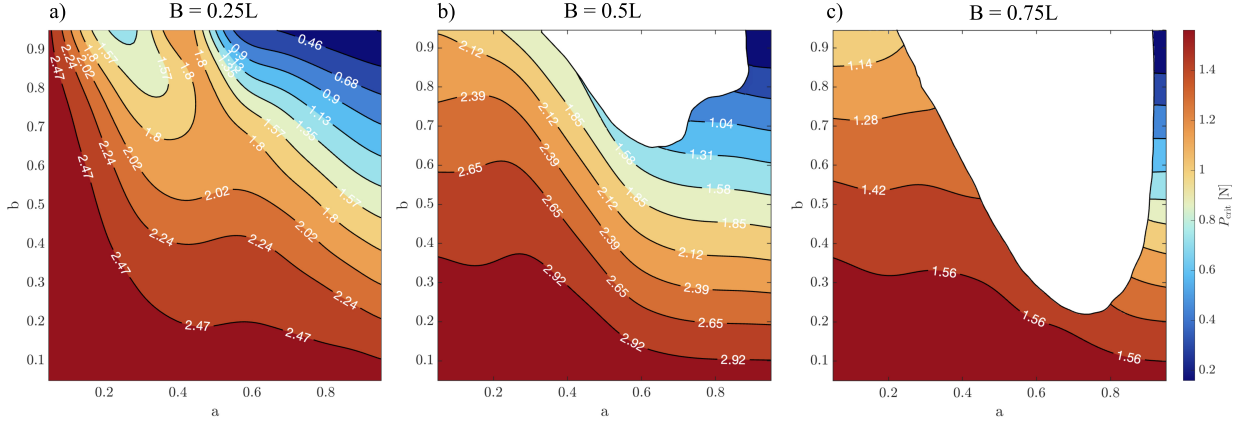


Figure 3: Critical value of the load in terms of the pattern parameters a and b . a) For $B = 0.25L$, all the patterns lead to stability loss. b) In case $B = 0.5L$, there is no stability loss in the white region. c) In case $B = 0.75L$, there is no stability loss in the white region.

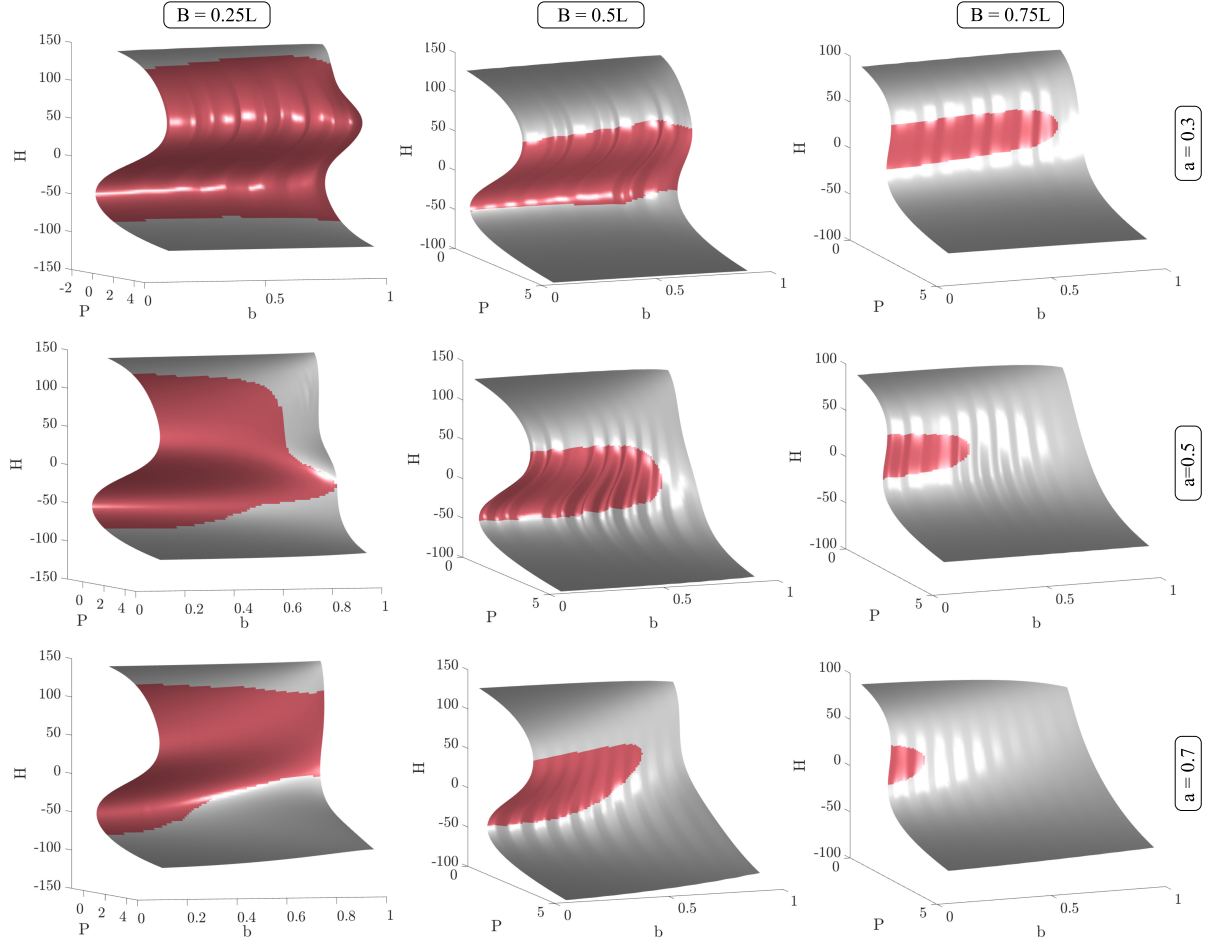


Figure 4: Shaded illustration of equilibrium surfaces for different a parameters (rows) and B support distances (columns). Grey and red colors correspond to stable and unstable states, respectively.

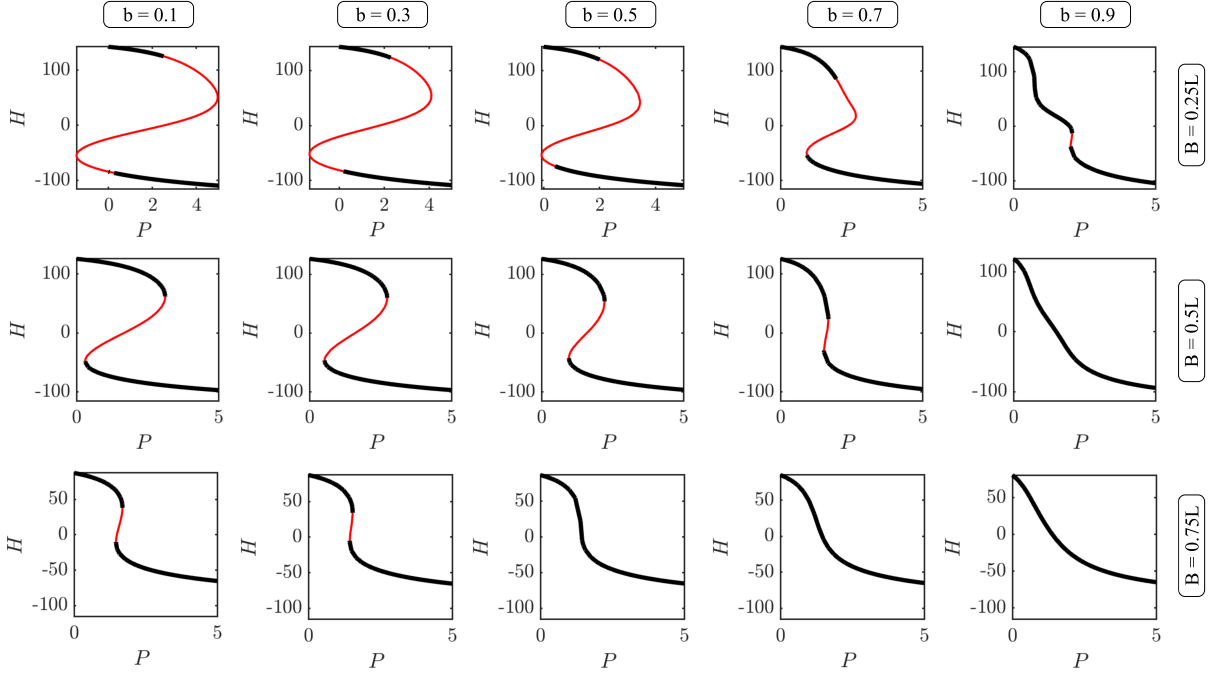


Figure 5: $P - H$ diagrams for different support distances (rows). The length of the cut, $a = 0.5$, was kept constant, and only the width, b , changed (columns). Black and red correspond to stable and unstable configurations, respectively.

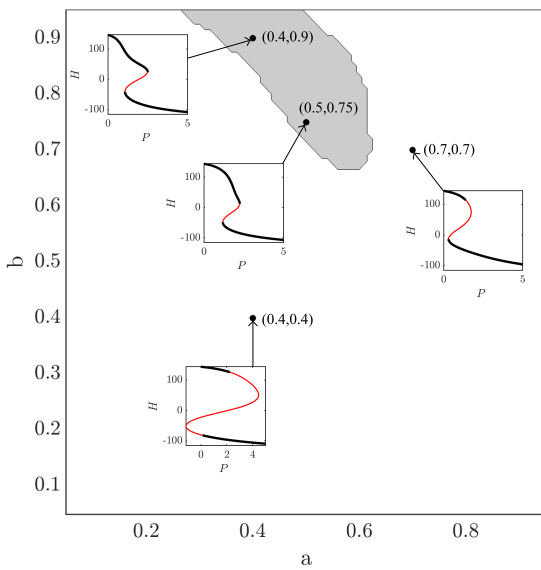


Figure 6: Grey zone corresponds to a and b parameters that exhibit limit point bifurcation, while the structure goes through symmetry point bifurcation outside the grey zone. The $P - H$ branch for some representative parameter combinations is shown in the inset figures, where red and black indicate unstable and stable configurations, respectively.

branch initially contains stable asymmetric states and the structure subsequently loses stability at a limit point. The corresponding structural shapes for the symmetric and asymmetric branches are shown in Fig. 7b and c, respectively. Notably, the two branches do not reconnect because of the loop formed in the asymmetric configuration.

These findings suggest that, in a load-controlled experiment with sufficiently small load increments, the structure would naturally transition onto the asymmetric branch. The lower stable portions of each path are physically inadmissible because the structure intersects itself. Determining the physically realizable configurations would require solving the constrained elastica problem, which lies beyond the scope of this work.

Enforcing symmetric snap-through rather than asymmetric buckling is achieved by softening the middle region of the structure. It allows the arch to deflect more under the same load, bringing it closer to the inverted configuration and enforcing symmetric stability loss. Without sufficient cuts, the structure undergoes asymmetric buckling. There are two competing effects: while cuts soften the structure, they also reduce the critical load. Consequently, only a limited range of cut sizes can induce symmetric snap-through. If the cuts are too

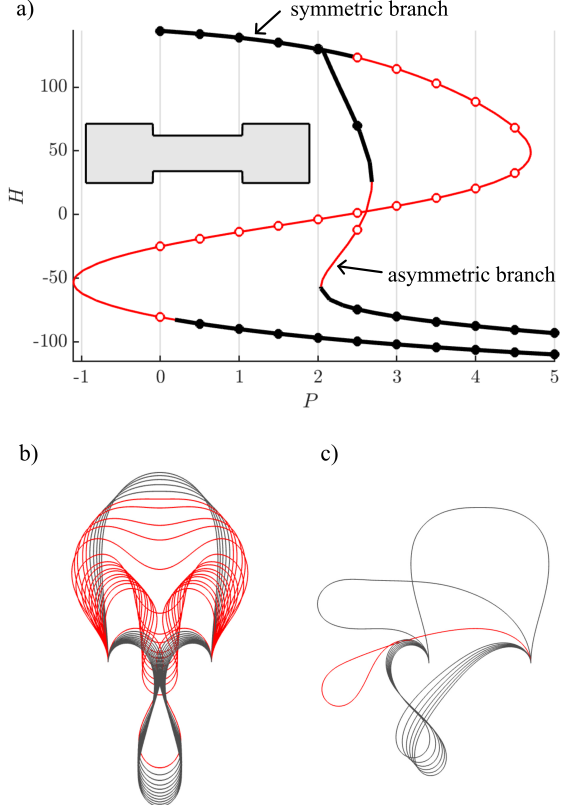


Figure 7: Numerical results of the pattern $a = 0.4$, $b = 0.4$. a) Symmetric and asymmetric branches of the $P - H$ diagram. Black and red color corresponds to stable and unstable states, respectively. The inset visualizes the pattern. b) Stable and unstable shapes (black and red, respectively) corresponding to the marked points on the symmetric branch. c) Stable and unstable shapes (black and red, respectively) corresponding to the marked points on the asymmetric branch.

large, the critical load associated with the limit-point bifurcation becomes so low that the softening effect is suppressed.

3.4. Experiments

The experiments were performed on laser-cut PET sheets with thickness $t = 0.5$ mm. The Young's modulus of the sheet is $E = 2800$ N/mm² (Vegt, van der and Govaert, 2003), and the density $\rho = 1.33$ g/cm³ was specified by the manufacturer. Three cut patterns were selected, all with fixed cut length $a = 0.5$ and varying cut heights $b = 0.2, 0.5, 0.8$. Each pattern was tested for three support distances $B = 0.25L, 0.5L$, and $0.75L$. The bounding rectangle of the patterns were 360x90 mm, with 10 mm used for the clamps at each end, leaving $L = 340$ mm, $W = 90$ mm. A small hole of 1 mm radius

was cut at the center of the sheet to accommodate the load, which was neglected in the calculations.

The load was applied on the arches in 0.5 N steps. The height of the structure was measured at the center of the sheet, using a measuring bar placed next to the structure. We photographed the structure and measured the height at each load step. After reaching the highest load level, the structure was unloaded in 0.5 N steps to capture the lower stable branch and the snap-back behavior.

We begin by discussing the cases exhibiting a limit-point bifurcation. Fig. 8 compares the numerical predictions and experimental results for $B = 0.5L$. The measured heights are plotted along with the calculated $P - H$ diagram in Fig. 8a-c. Overall, there is a good agreement between the calculations and the experimental data. The largest differences occur near the bifurcation points, likely due to their sensitivity to small inaccuracies in the cut pattern, the applied load, or the load position. The calculated structural shapes also closely match the photographs (Fig. 8d-f), and the structure remained symmetric at each load level. For $b = 0.8$ (Fig. 8c), no snap-through or snap-back was observed, i.e., the loading and unloading paths coincided. This behavior is consistent with the numerical predictions, which indicate monotonic monostability for this pattern.

The case of $B = 0.75L$ also showed good agreement between numerical predictions and experimental results (Fig. 9). Only $b = 0.2$ exhibited snap-through, with the largest differences between the calculations and experiments occurring near the bifurcation point (Fig. 9 a). For $b = 0.5$, no snap-through was observed; however, the middle part of the diagram is very steep, which corresponds to the region of largest deviation between experiments and calculations. Regions with gentler slopes exhibited better agreement. The closest agreement was achieved for $b = 0.8$ (Fig. 9c), where the $P - H$ diagram is free from steep parts and stability loss. In the experiments, both $b = 0.5$ and $b = 0.8$ showed no snap-through or snap-back, in excellent agreement with the numerical predictions of monotonic monostability.

As discussed in Subsection 3.3, the case of $B = 0.25L$ is more complex. The selected b values include both limit point and symmetry point bifurcations. Additionally, at high load levels, some solutions become physically unfeasible due to self-intersections. Our experimental setup also imposed a constraint on the horizontal displacement of the arch, preventing testing at the highest load levels.

Figure 10a,b shows the load-height diagrams for $b = 0.2$ and $b = 0.5$, including both symmetric and asymmetric branches. The corresponding experimental and

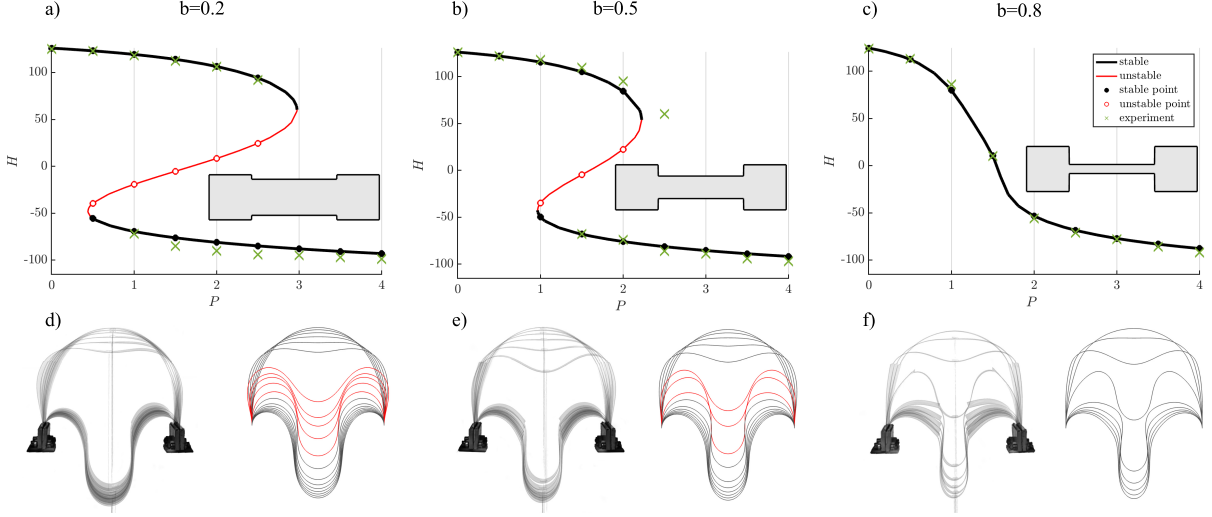


Figure 8: Experimental and numerical results for $B = 0.5L$. The length of the cut was kept $a = 0.5$. a-c) Force-height diagrams for different cut heights. Black and red lines correspond to stable and unstable points, respectively. The markers are placed in $0.5 N$ steps. Black and red circular markers correspond to stable and unstable points, respectively. Green 'x' denotes the measured height values. The inset illustrates the cut pattern. a) $b = 0.2$, b) $b = 0.5$, c) $b = 0.8$. d-f) Photographs (left) and calculated shapes (right) corresponding to the markers. Red shows unstable shapes. d) $b = 0.2$, e) $b = 0.5$, f) $b = 0.8$.

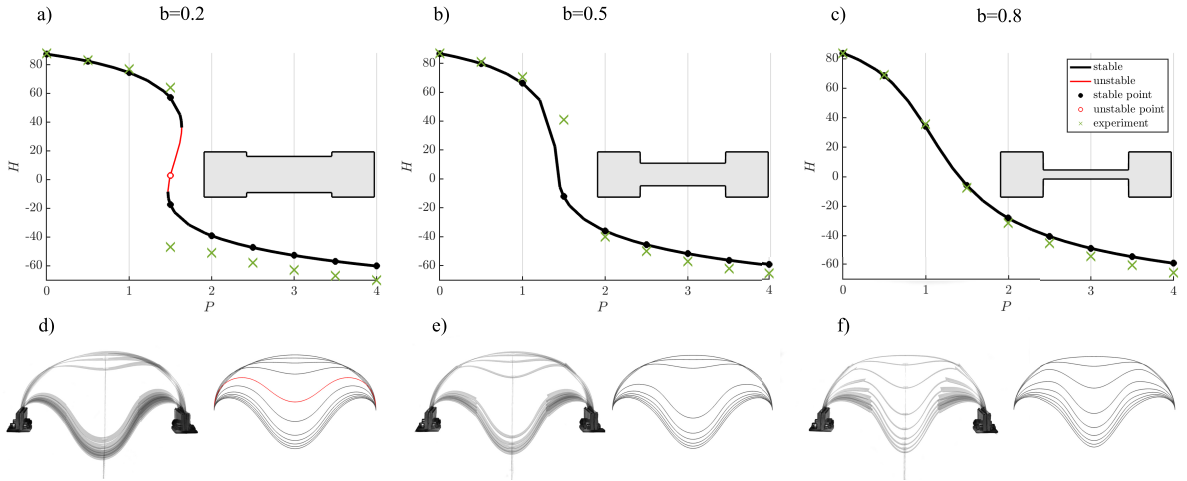


Figure 9: Experimental and numerical results for $B = 0.75L$. The length of the cut was kept $a = 0.5$. a-c) Force-height diagrams for different cut heights. Black and red lines correspond to stable and unstable points, respectively. The markers are placed in $0.5 N$ steps. Black and red circular markers correspond to stable and unstable points, respectively. Green 'x' denotes the measured height values. The inset illustrates the cut pattern. a) $b = 0.2$, b) $b = 0.5$, c) $b = 0.8$. d-f) Photographs (left) and calculated shapes (right) corresponding to the markers. Red shows unstable shapes. d) $b = 0.2$, e) $b = 0.5$, f) $b = 0.8$.

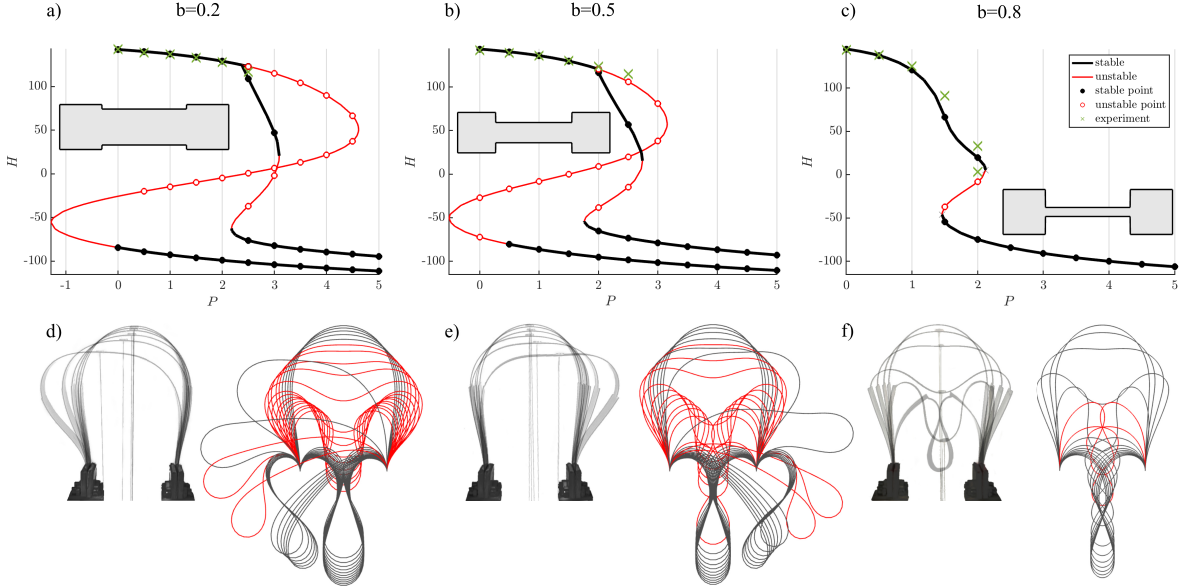


Figure 10: Experimental and numerical results for $B = 0.25L$. The length of the cut was kept $a = 0.5$. a)-c) Force-height diagrams for different cut heights. Black and red lines correspond to stable and unstable points, respectively. The markers are placed in 0.5 steps. Black and red circular markers correspond to stable and unstable points, respectively. Green 'x' denotes the measured height values. The inset illustrates the cut pattern. a) $b = 0.2$, b) $b = 0.5$, c) $b = 0.8$. d)-f) Photographs (left) and calculated shapes (right) corresponding to the markers. Red shows unstable shapes. d) $b = 0.2$, e) $b = 0.5$, f) $b = 0.8$.

calculated shapes are shown in Fig. 10d,e. All calculated symmetric and asymmetric shapes are overlaid for comparison. The photographs reveal that the structure initially follows the symmetric branch; once the symmetric shape loses stability, it transitions to an asymmetric configuration. Further loading was limited by the horizontal displacement constraint in the experiments.

The lower stable branches of the $P - H$ diagrams in Fig. 10 contain self-intersections or contacting parts. Consequently, we could compare only the upper parts of the diagrams to experiments. The experiments and calculations agreed well, the largest difference occurred near the bifurcation points.

Figure 10c corresponds to a case with limit point bifurcation, where the structure remained symmetric in both the experiments and the calculations. The calculated and measured heights agree well, and the largest differences occur near the steep parts of the diagram. The structural shapes also match closely (Fig. 10f). The photographs show that the last shape (corresponding to $P = 2$ N) has contacting parts, indicating that the assumptions of the model no longer hold beyond this point.

4. Conclusion

The results reveal an interesting phenomenon: by carefully designing the cut patterns, it is possible to control the mode of stability loss for kirigami arches under vertical loads. We demonstrated examples in which snap-through disappears for certain cut patterns, as well as cases in which cuts enforce symmetric stability loss. As a result, cuts can significantly alter the overall stability characteristics.

For larger support distances ($B = 0.5L$ and $B = 0.75L$), the structure goes through snap-through at a limit point bifurcation in general, but the limit point disappears for certain a and b parameter pairs and the structure goes to the inverted position through stable shapes without exhibiting snap-through. Therefore, introducing cuts can suppress stability loss and enforce monotonic monostability.

For $B = 0.25L$, the symmetric shape loses stability and the physically observable equilibrium path is the asymmetric path for a wide range of parameters. However, there is a small range of cut patterns that keeps the symmetric path stable until the limit point, leading to a limit point bifurcation. As a result, cuts can enforce symmetric stability loss.

In summary, we identified patterns with limit point bifurcation, symmetry point bifurcation, and monotonic

monostability. The phenomena observed here arise from multiple competing effects, including local softening, and structural shape.

Overall, our results highlight the potential of kirigami techniques to tailor the stability behavior of kirigami-inspired structures. In addition to the behaviors studied here, we could expect bistable, multistable, or more complex responses for more intricate cut patterns. The results can be applied to adjustable energy absorbers, deployable structures, and energy harvesting systems. Future work could explore the simultaneous optimization of geometry and mechanical response to achieve desired stability characteristics in kirigami-inspired systems.

Acknowledgments

We acknowledge the Digital Government Development and Project Management Ltd. for awarding us access to the Komondor HPC facility based in Hungary. This research was supported by the NKFIH Hungarian Research Fund Grants 143175. This research was conducted with the support of the ERASMUS+ Programme of the European Union.

References

Chen, J.S., Hung, S.Y., 2011. Snapping of an elastica under various loading mechanisms. *European Journal of Mechanics-A/Solids* 30, 525–531.

Cheng, X., Xu, S., Jin, T., Shen, Z., Zhang, Y., 2023. Bifurcation and mode transition of buckled ribbons under oblique compressions. *Mechanics Research Communications* 131, 104145.

Cho, H., Kim, D.N., 2023. Controlling the stiffness of bistable kirigami surfaces via spatially varying hinges. *Materials and Design* 231. doi:10.1016/j.matdes.2023.112053.

Dohnal, T., Rademacher, J.D., Uecker, H., Wetzel, D., 2014. pde2path 2.0: multi-parameter continuation and periodic domains, in: Proceedings of the 8th European Nonlinear Dynamics Conference, ENOC.

Driscoll, T.A., Hale, N., Trefethen, L.N., 2014. Chebfun guide .

Du, C., Wang, Y., Kang, Z., 2024. Cut layout optimization for design of kirigami metamaterials under large stretching. *Theoretical and Applied Mechanics Letters* 14, 100528.

Fehér, E., 2025. Rigidity paradox of kirigami arches. *arXiv preprint arXiv:2508.09310* .

Fehér, E., Gyetvai, Z., 2024. Tailoring rigidity of bending-active perforated sheets, in: Block, P., Boller, G., DeWolf, C., Pauli, J., Kauffmann, W. (Eds.), *Proceedings of IASS Annual Symposia, International Association for Shell and Spatial Structures (IASS)*. p. 549.

Fehér, E., Sipos, A.Á., Várkonyi, P., 2026. Quasi-static shape control of structures with topologically complex equilibrium sets. *European Journal of Mechanics - A/Solids* 117, 106000. doi:<https://doi.org/10.1016/j.euromechsol.2025.106000>.

Gomez, M., Moulton, D.E., Vella, D., 2017. Critical slowing down in purely elastic ‘snap-through’ instabilities. *Nature Physics* 13, 142–145.

Hamzehei, R., Bodaghi, M., Wu, N., 2024. Mastering the art of designing mechanical metamaterials with quasi-zero stiffness for passive vibration isolation: a review. *Smart Materials and Structures* 33, 083001.

Hong, Y., Chi, Y., Wu, S., Li, Y., Zhu, Y., Yin, J., 2022. Boundary curvature guided programmable shape-morphing kirigami sheets. *Nature Communications* 13. doi:10.1038/s41467-022-28187-x.

Howell, P., Kozyreff, G., Ockendon, J., 2009. *Applied solid mechanics*. 43, Cambridge University Press.

Lee, T.U., Gattas, J.M., Xie, Y.M., 2022. Bending-active kirigami. *International Journal of Solids and Structures* 254–255, 111864. doi:10.1016/j.ijsolstr.2022.111864.

Li, H., Zhang, W., Liao, X., Xu, L., 2024. Kirigami enabled reconfigurable three-dimensional evaporator arrays for dynamic solar tracking and high efficiency desalination. *Science Advances* 10, eado1019.

Liu, J., Jiang, S., Xiong, W., Zhu, C., Li, K., Huang, Y., 2022. Self-healing kirigami assembly strategy for conformal electronics. *Advanced Functional Materials* 32, 2109214.

Liu, M., Domino, L., Vella, D., 2020. Tapered elasticæ as a route for axisymmetric morphing structures. *Soft Matter* 16, 7739–7750.

Liu, S., Burgueño, R., 2016. Controlled elastic postbuckling of bilaterally constrained non-prismatic columns: application to enhanced quasi-static energy harvesters. *Smart Materials and Structures* 25, 125010.

Luu, A.T., Lee, J., 2016. Non-linear buckling of elliptical curved beams. *International Journal of Non-Linear Mechanics* 82, 132–143.

Pedivellano, A., Pellegrino, S., 2024. Folding kinematics of kirigami-inspired space structures. *International Journal of Solids and Structures* 300, 112865.

Pi, Y.L., Bradford, M., Uy, B., 2002. In-plane stability of arches. *International Journal of Solids and Structures* 39, 105–125.

Pi, Y.L., Trahair, N., 1998. Non-linear buckling and postbuckling of elastic arches. *Engineering Structures* 20, 571–579.

Rafsanjani, A., Bertoldi, K., 2017. Buckling-induced kirigami. *Physical review letters* 118, 084301.

Shrimali, B., Pezzulla, M., Poincloux, S., Reis, P.M., Lopez-Pamies, O., 2021. The remarkable bending properties of perforated plates. *Journal of the Mechanics and Physics of Solids* 154, 104514.

Stein-Montalvo, L., Ding, L., Hultmark, M., Adriaenssens, S., BouZeid, E., 2024. Kirigami-inspired wind steering for natural ventilation. *Journal of Wind Engineering and Industrial Aerodynamics* 246, 105667.

Tao, J., Khosravi, H., Deshpande, V., Li, S., 2023. Engineering by cuts: How kirigami principle enables unique mechanical properties and functionalities. doi:10.1002/advs.202204733.

Thompson, J.M.T., Hunt, G.W., 1973. A general theory of elastic stability. (No Title) .

Timoshenko, S.P., Gere, J.M., 1961. *Theory of elastic stability*, 2nd ed. McGraw-Hill.

Trefethen, L.N., 2000. *Spectral methods in MATLAB*. SIAM.

Uecker, H., 2021. Numerical continuation and bifurcation in Nonlinear PDEs. SIAM.

Vegt, van der, A., Govaert, L., 2003. *Polymeren : van keten tot kunststof*. 5e dr. / a.k. van der vegt en i.e. govaert ed., DUP Blue Print.

Wu, J., Guo, X., Pan, X., Hua, J., Cen, Y., Li, S., Huang, F., Zhang, F., Pan, L., Shi, Y., 2025. Origami-kirigami structures and its applications in biomedical devices. *Biomedical Materials & Devices* 3, 45–61.

Yang, Y., Feng, J., Holmes, D.P., 2024. Mechanical computing with transmissive snapping of kirigami shells. *Advanced Functional Materials* 34, 2403622.

Zhang, Y., Huang, W., Liu, M., Yu, J., Gao, H., 2025. Snap-through buckling in heavy hard magnetic elastica. *Proceedings of the Royal*

Society A 481, 20250008.

Zhang, Y., Jiao, Y., Wu, J., Ma, Y., Feng, X., 2020. Configurations evolution of a buckled ribbon in response to out-of-plane loading. *Extreme Mechanics Letters* 34, 100604.

Zhang, Y., Yang, J., Liu, M., Vella, D., 2022. Shape-morphing structures based on perforated kirigami. *Extreme Mechanics Letters* 56. doi:10.1016/j.eml.2022.101857.